Supporting Information

Fabrication of Diffraction Gratings by Top-Down and Bottom-Up Approaches Based on Scanning Probe Lithography†

Mi-Sun Yang,[‡a] Changhoon Song, [‡a] Jihoon Choi,[b] Jeong-Sik Jo,[a] Jin-Hyun Choi,[a] Byung Kee Moon,[a] Heeso Noh,*[b] and Jae-Won Jang*[a]

[a]Department of Physics, Pukyong National University, 45 Yongso-ro, Nam-gu, Busan 48513, Korea
*E-mail: jjang@pknu.ac.kr; jjang@pukyong.ac.kr
[b]Department of Nano and Electronic Physics, Kookmin University, Seoul, 02707, Republic of Korea
*E-mail: heesonoh@kookmin.ac.kr

‡ The authors contributed equally to this work.

I. Filling-factor-dependent reflectance of silicon diffraction gratings

Performance of the silicon diffraction gratings fabricated by the top-down approach is characterized in terms of the filling factor of the diffractors in the gratings, as shown in Figure S1. The filing factor (A_D/A_G) is defined as the ratio of the area of the diffractors (A_D) and the entire area of the grating (A_G). The A_D of the gratings in the pre-RIE step is determined as the area of Au dot arrays, while that of the gratings in the post-RIE step is determined as the area of nanocircular silicon pillars from the top view.

The filling factors were as follows for diffraction gratings with different lattice constants: 0.144 (700 nm), 0.071 (1000 nm), and 0.049 (1200 nm). In case of the gratings in the pre-RIE step (Figure S1(a)), the reflectance of the silicon diffraction gratings increases linearly with the filling factor. This means that the reflectance is enhanced with the number of the diffractors (with equal heights and the Au/Ti films with thicknesses of 35 nm). However, no dependence of the reflectance on the filling factor is observed in the case of the gratings in the post-RIE step (Figure S1(b)); thus, it appears that the filling factor does not significantly influence the reflectance of gratings in which the height of the diffractors is similar to the incidence wavelength. The reflectance shown in Figure S1(a) and S1(b) are averaged from the data shown in Figure 3. Figure S1(c) shows the filling-factor-dependent heights of the diffractors obtained by RIE processes (RIE depth). As the filling factor increases, the RIE depth decreases.
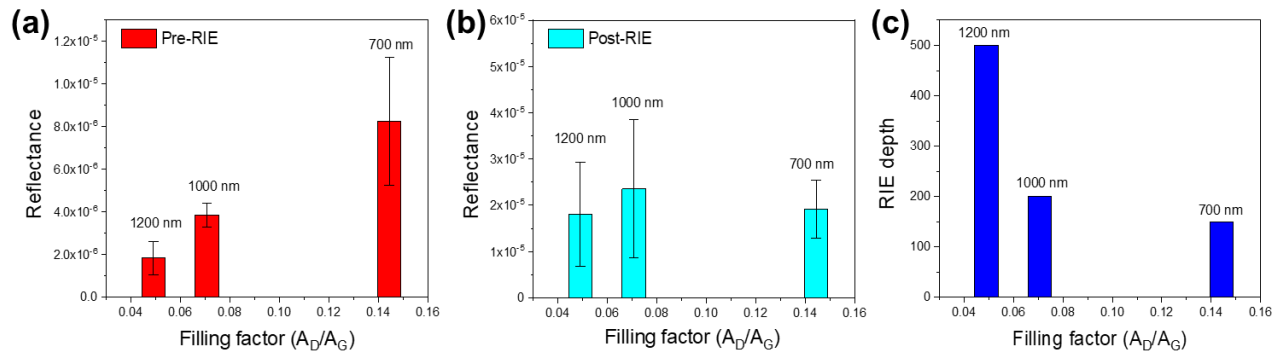
Figure S1. The filling-factor-dependent reflectance of the silicon diffraction gratings in the (a) pre-and (b) post-RIE steps. (c) The filling-factor-dependent height of the diffractors as obtained by the RIE process (RIE depth)

II. Optimized height of the diffractors in diffraction gratings

Suitable height of the diffractors for clearly observable diffraction (constructive interference condition) can be estimated under Bragg's condition, as shown in Figure S2. As the incident light is reflected on the top and bottom planes of the diffractors (Figure S2), the path difference (Δ_{path}) of the incidence "A" and "B" is determined as $2t\sin\theta$, where t is the height of the diffractors, and θ is the scattering angle. Hence, Bragg's condition will be Δ_{path} = $2t\sin\theta = m\lambda$, where m is an integer, and λ is the incidence wavelength. The following conditions are considered for observable diffractions: θ of 30°, 45°, 60°, and 90°, visible wavelength (λ = 400 − 700 nm), and the first mode (m = 1); hence, t should be 150–500 nm (θ = 30°), 213–710 nm (θ = 45°), 261–870 nm (θ = 60°), and 300–1000 nm (θ = 90°) to diffract visible light (λ = 400–700 nm). Considering the operating condition of the diffraction gratings, including white light incidence and bare-eye observation (wide-angle scattering), the suitable value of t is estimated as 500 nm; hence, the target depth during the RIE process is set as 500 nm.
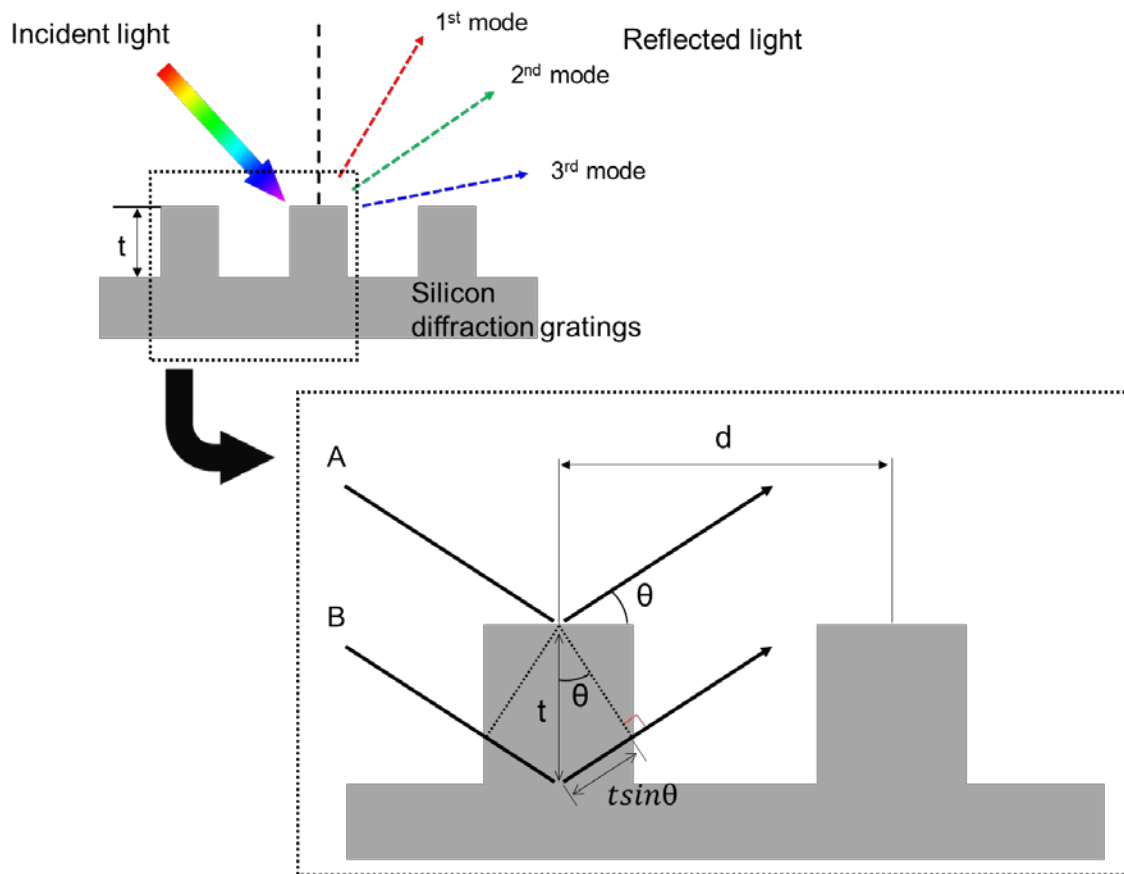
Figure S2. Schematic showing the diffraction conditions of the gratings

III. SEM images of the silicon diffraction gratings

Figure S3 shows an SEM image of the linearly elongated nanocircular silicon pillar array gratings with lattice constants of 1200, 1000, and 700 nm. One pen of the 1D pen array prints over areas of 35 μm × 40 μm, and these areas are well connected to each other, as shown in Figure S3. Finally, the *sc* lattice can be generated in an area of 600 μm × 40 μm by one set of DPN printing. Three sets of nanocircular silicon pillar array gratings with 12-μm spacing are well obtained, as shown in Figure S3.
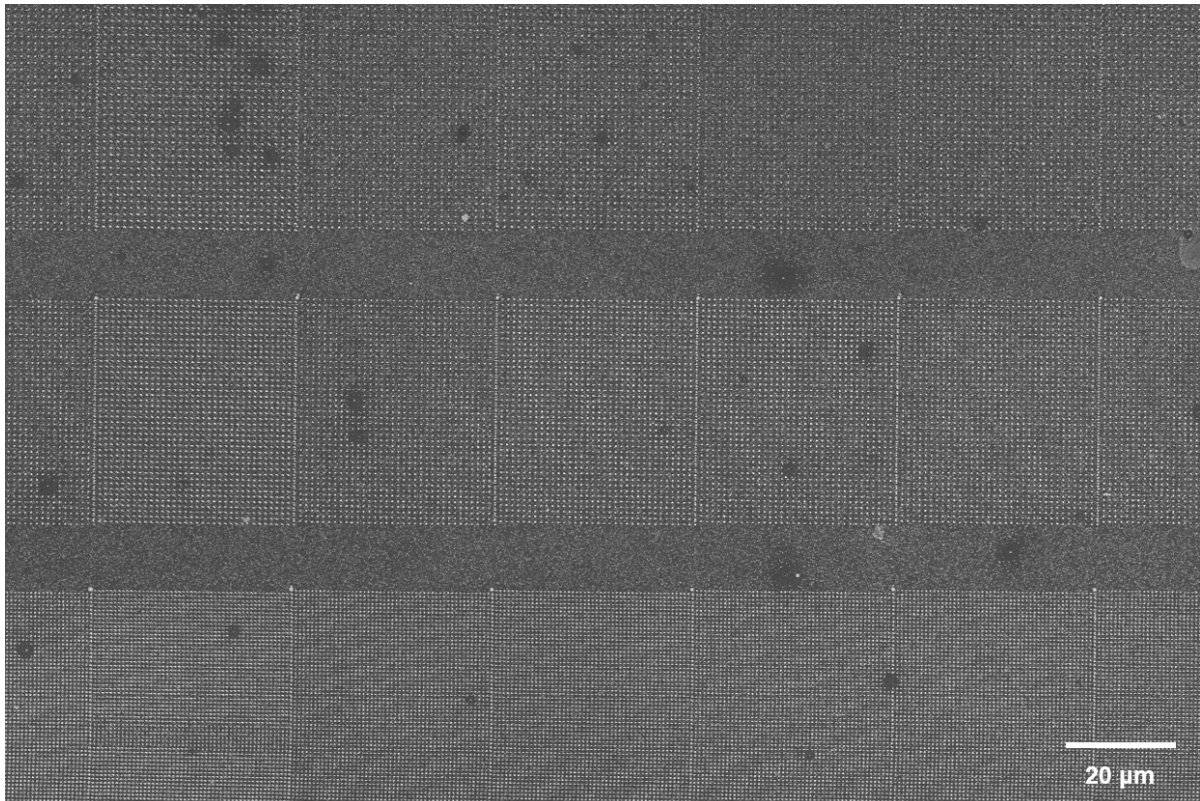

Figure S3. Scanning electron microscopy (SEM) image of the linearly elongated nanocircular silicon pillar array gratings with lattice constants of 1200 (top), 1000 (central), and 700 nm (bottom).

IV. Silicon diffraction gratings in the pre-RIE process

Field emission SEM (FE-SEM) images of the diffraction gratings fabricated by the top-down approach are measured, as shown in Figure S4. FE-SEM images of the gratings with lattice constants of 700, 1000, and 1200 nm in the pre-RIE step are shown in Figure S4(a), S4(b), and S4(c), respectively. Figure S4(d), S4(e), and S4(f) show the FE-SEM images of gratings with lattice constants of 700, 1000, and 1200 nm, respectively, in the post-RIE step. All the FE-SEM images are obtained from independent samples.
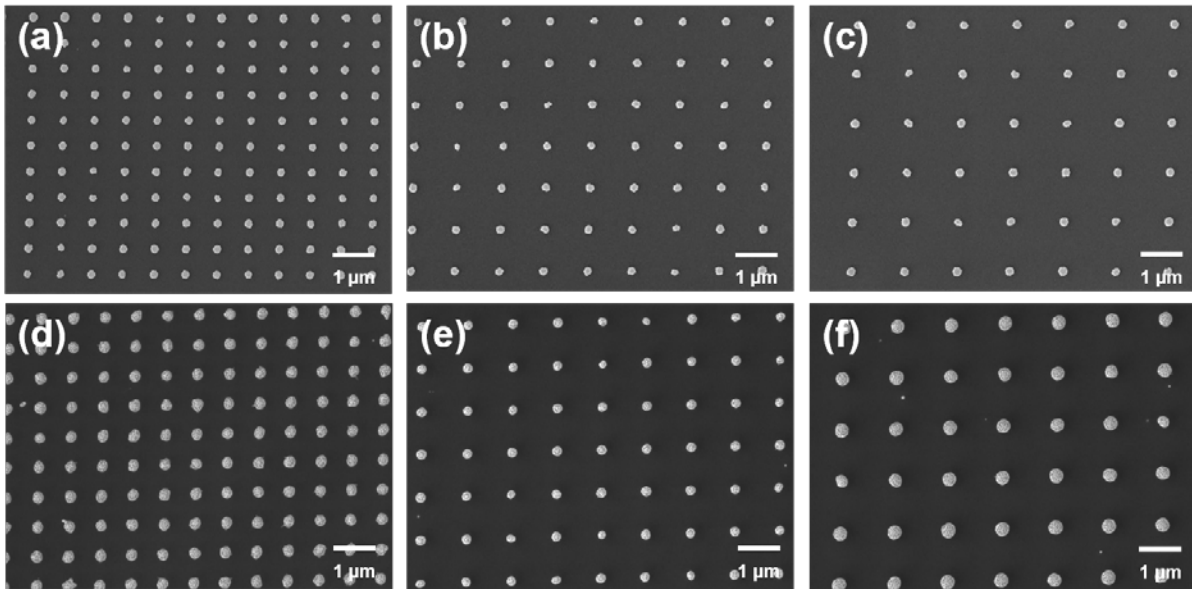

Figure S4. Field emission scanning electron microscopy (FE-SEM) images of the diffraction gratings fabricated by the top-down approach in the (a–c) pre-RIE and (d–f) post-RIE steps. The lattice constants of the gratings are 700 (a, d), 1000 (b, e), and 1200 nm (c, f).

V. Detailed configuration for measuring the performances of the diffraction gratings

Instrumental configurations for the diffraction measurements of the nanocircular silicon pillars and ZrO_2 NP diffraction gratings are well described, as shown in Figures S5 and S6, respectively. In the case of the measurement of the nanocircular silicon pillar diffraction grating, light from a tungsten halogen lamp (ASB-W-020R, Korea Spectral Products, Korea) with an aperture of $\phi = 0.5$ mm was focused onto the sample with a focusing angle of 2° by using a combination of two lenses. A lens (f = 150 mm, $\phi = 25.4$ mm) was used to collect the diffracted light from the sample, as shown in Figure S5. A spectrometer (SM245, Korea Spectral Products, Korea) was used as the detector. For the self-assembled ZrO_2 NP diffraction grating, laser light ($\lambda = 687$ nm, RLT6830MG, Roithner Lasertechnik, Austria) with an aperture of $\phi = 0.5$ mm was focused on the sample with a focusing angle of 0.03° (Figure S6). In addition, laser light ($\lambda = 405$ nm, DL5146-101S, Thorlabs Inc., U.S.A.) with same configuration shown in Figure S6 was also used for the measurements of the incidence-angle-dependent diffraction intensity of the linearly elongated nanocircular silicon pillar diffraction grating (Figure 4).
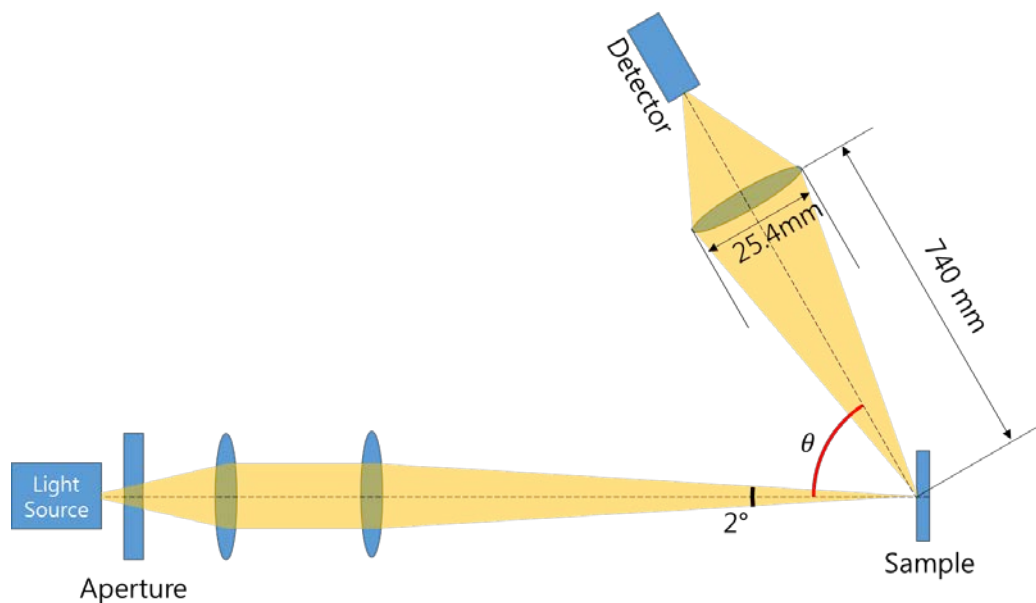
Figure S5. Instrumental configurations for the diffraction measurement of the nanocircular silicon pillar diffraction grating.
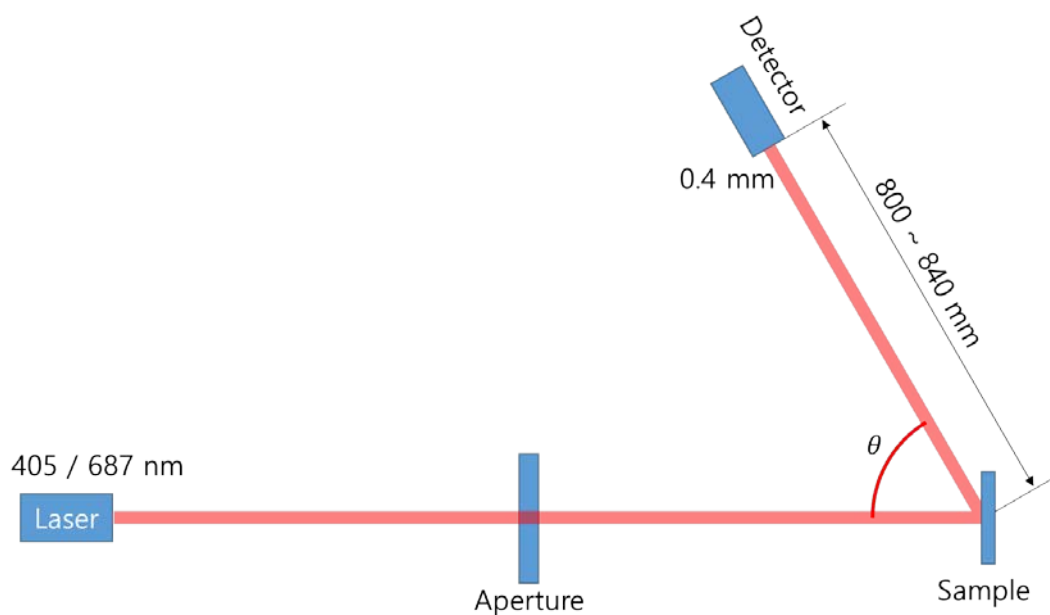

Figure S6. Instrumental configurations for the diffraction measurement of the ZrO$_2$ NP diffraction grating ($\lambda = 687$ nm) and for the incidence-angle-dependent diffraction intensity of the linearly elongated nanocircular silicon pillar diffraction grating ($\lambda = 405$ nm).

VI. Incidence-angle-dependent color representation of the microspectrometer

The incidence-angle-dependent diffraction of the linearly elongated nanocircular silicon pillar array gratings (the gratings of the microspectrometer) was measured. The grating was placed on the goniostage (-15° to 15° adjustment, GN05, Thorlabs Inc., U.S.A.) mounted on a 45° tilting sample stage in the optical microscope (OM) (Axio scope A1, Carl Zeiss, Germany) (Figure S7); hence, the incidence angle could be controlled by means of the goniostage with and without tilting the sample stage from 0° to 60°. The RGB color image (Figure 3(e)) of the linearly elongated nanocircular silicon pillar array gratings was measured using the florescence (FL) mode of the OM and was obtained by merging the individual red (filter set 45, Carl Zeiss, Germany), green (filter set 44, Carl Zeiss, Germany), and blue (filter set 49, Carl Zeiss, Germany)-filtered images with white light incident at 45° (mercury arc lamp, HBO 50, Carl Zeiss, Germany). The same exposure times (700 ms) were used for the individual RGB FL imaging.

The OM images (FL mode) of the silicon diffraction gratings with lattice constants of 700 nm and 1200 nm in range of incidence angle from 30° to 60° are shown in Figure S8(a) and S8(b), respectively.
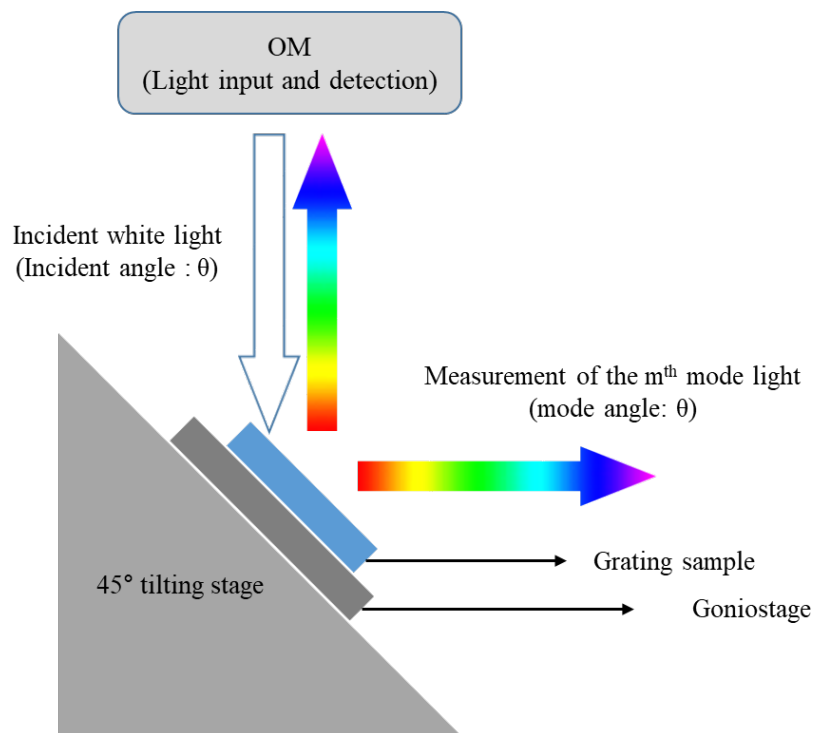
Figure S7. Measurement of the incidence-angle dependent diffraction of the linearly elongated silicon nanocircular pillar array gratings.
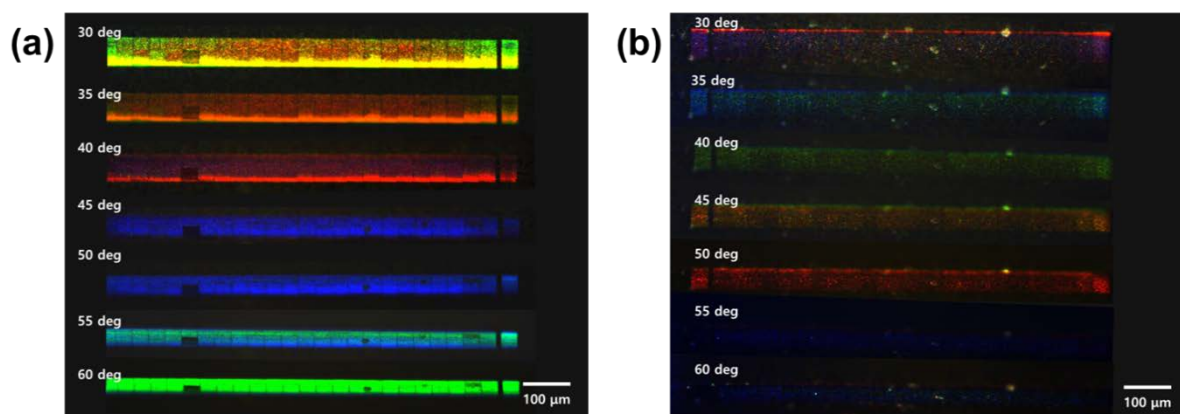

Figure S8. OM images obtained in the florescence mode of the silicon diffraction gratings with lattice constants of (a) 700 nm and (b) 1200 nm for different incidence angles. In the images, the measurements for all the incidence angles are shown for convenient comparison.

11

VII. Optical image of the entire ZrO$_2$ NP diffraction grating

To prove that self-assembled ZrO$_2$ NP diffraction gratings over the millimeter scale were fabricated, the OM image of the ZrO$_2$ NP diffraction grating is shown in Figure S9. The OM image was obtained by merging individually captured images (100 ×) in the dark-mode. The ZrO$_2$ NPs are well assembled in a relatively large area, corresponding to size of the PPL stamp (5 mm × 5 mm), with a lattice constant of 40 μm.
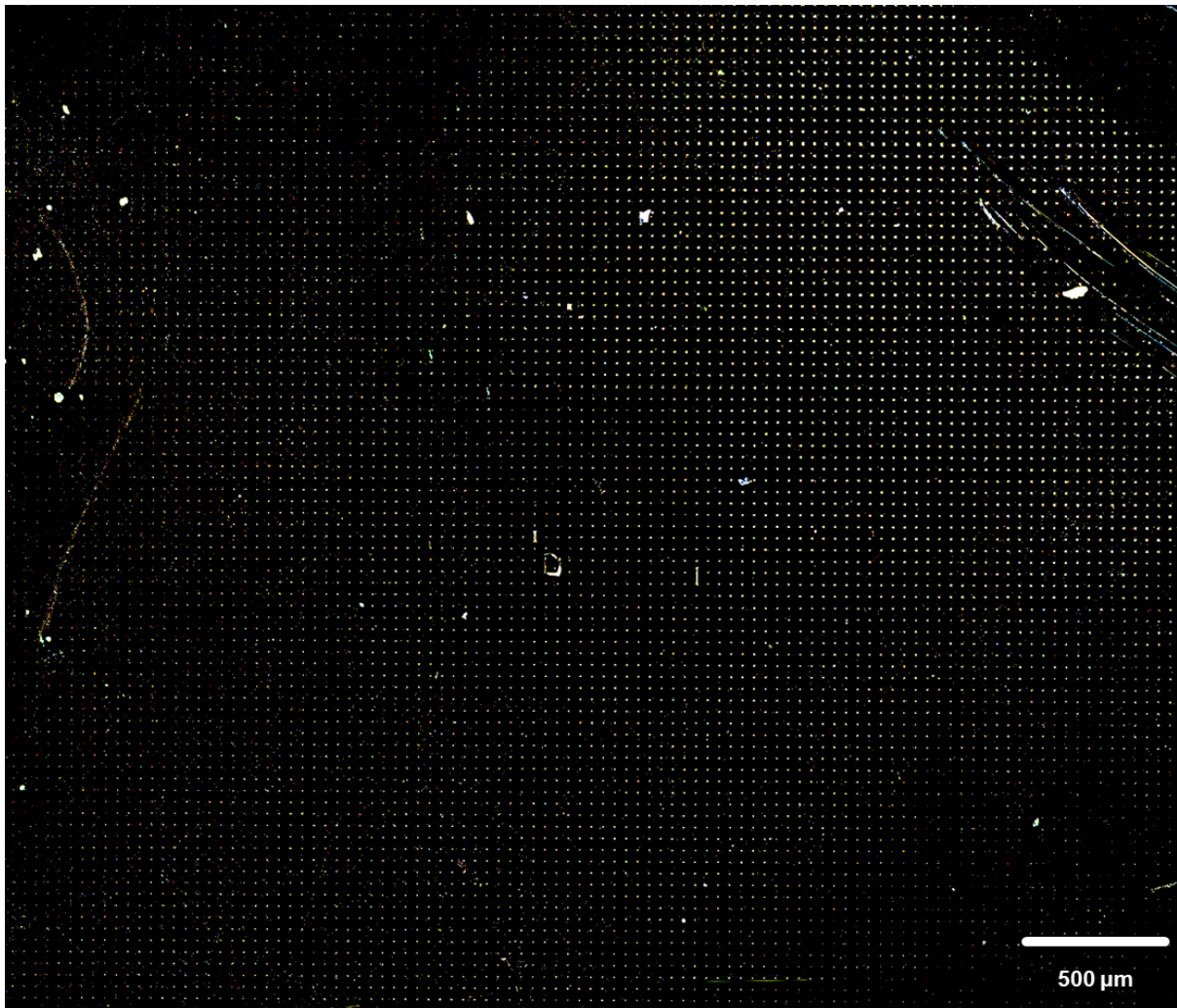

Figure S9. Optical microscopy image (dark-mode) of the self-assembled ZrO$_2$ NP diffraction grating fabricated in a relatively large area.

VIII. Size distribution of the ZrO$_2$ NPs

The size distribution of the ZrO$_2$ NPs used in the diffraction grating fabricated by the bottom-up approach was characterized by using a laser diffraction particle size analyzer (ELS8000, OTSUKA Electronics, Japan). Aqueous ZrO$_2$ NP solution (4 mM/mL) was prepared and sonicated for one hour before the characterization to prevent aggregation of the ZrO$_2$ NPs. Figure S10 shows a histogram of the diameter of the ZrO$_2$ NPs measured by the laser diffraction particle size analyzer. The mean diameter of the ZrO$_2$ NPs is 474.4 nm with a standard deviation of 143.3 nm (474.4 ± 143.3 nm). As a complementary characterization, the diameter of the ZrO$_2$ NPs is measured from an FE-SEM image of the ZrO$_2$ NPs (Figure S11(a)). Figure S11(b) shows that the mean diameter of the ZrO$_2$ NPs obtained from the histogram is 488.7 ± 56.5 nm.
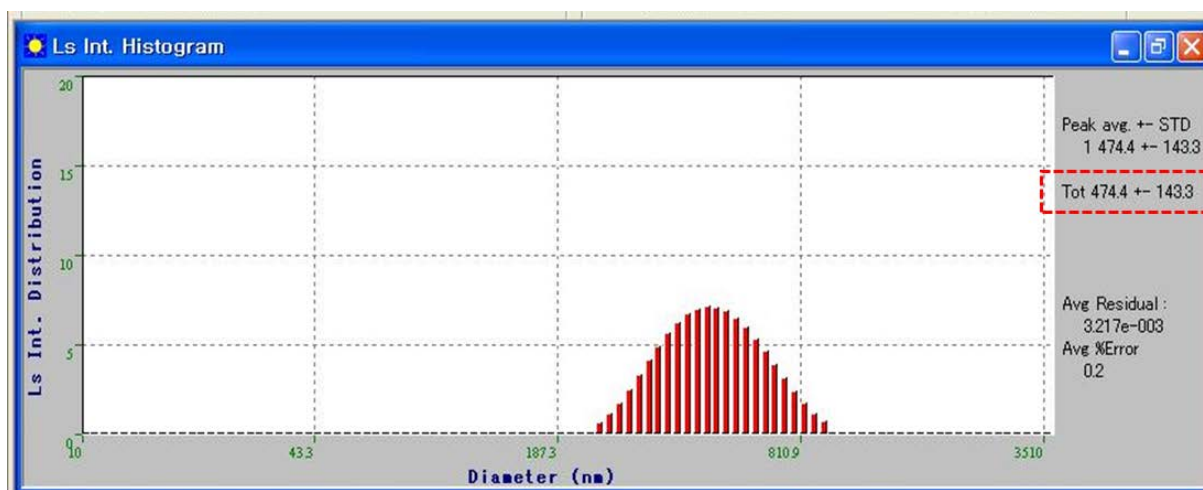

Figure S10. Screenshot of the histogram of diameter of the ZrO$_2$ NPs. The red-dashed box represents the mean of the measured diameters with the standard deviation.
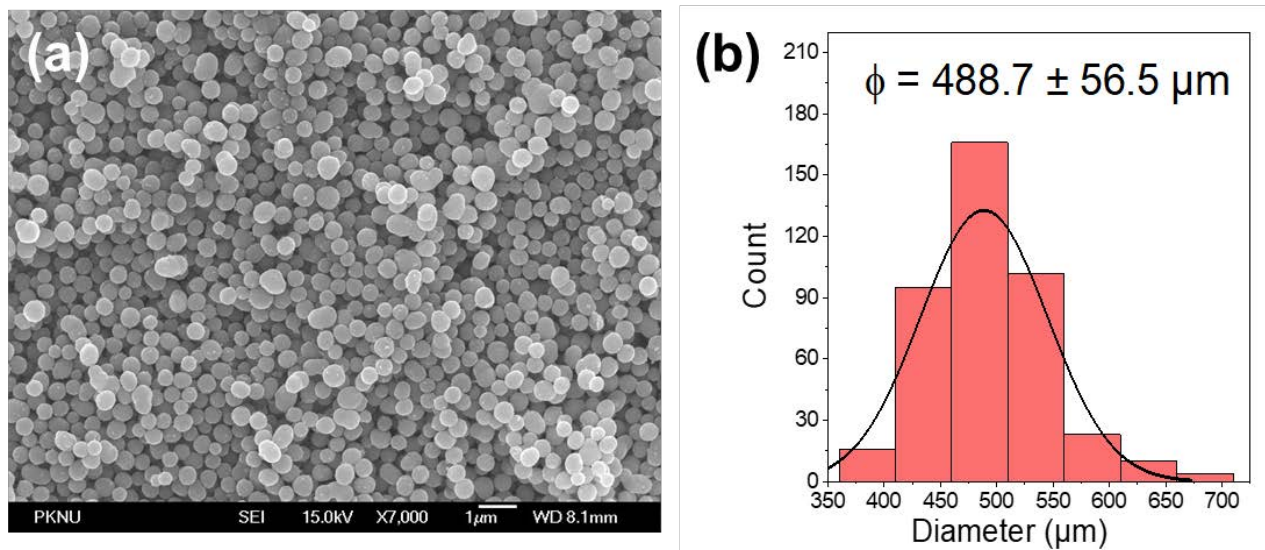
Figure S11. (a) FE-SEM image of the ZrO_2 NPs. (b) A histogram of diameter of the ZrO_2 NPs obtained from (a). In all, 416 ZrO_2 NPs were measured to obtain the histogram.

IX. SEM images of the ZrO$_2$ NP diffraction grating

In Figure S12(a), a SEM image of the ZrO$_2$ NP diffraction grating is shown. To carefully characterize configuration of ZrO$_2$ NPs at the lattice points, zoomed SEM images measured in certain lattice points (denoted as "i" – "vi" in Figure S12(a)) are measured and displayed as shown in Figure S12(b). Density of the ZrO$_2$ NPs at the lattice points is low, and the ZrO$_2$ NPs are randomly positioned. However, the ZrO$_2$ NPs seem to be located within square area.
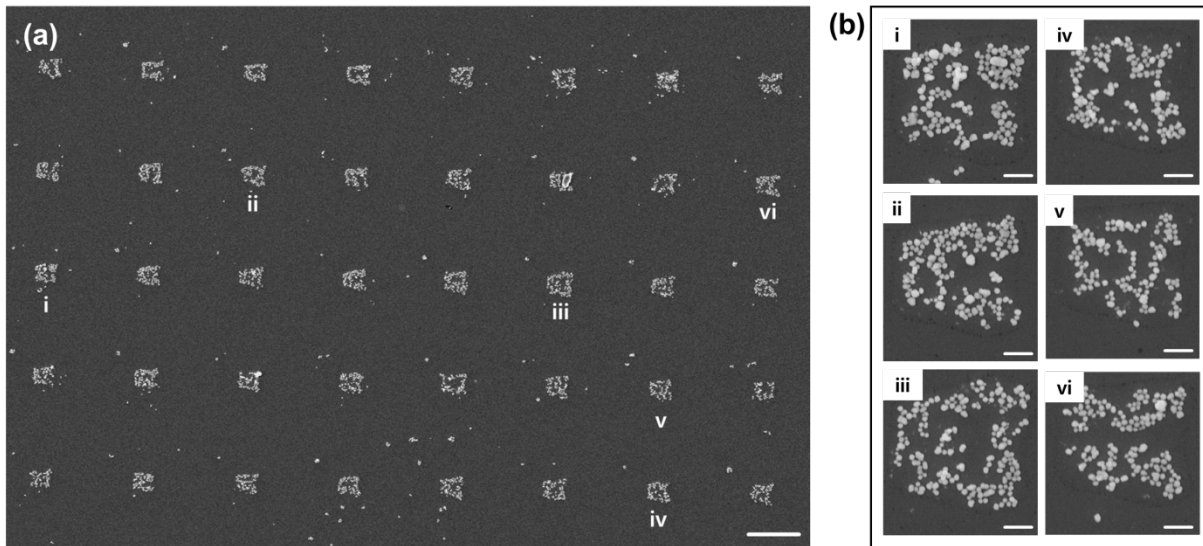

Figure S12. (a) An SEM image of the ZrO$_2$ NP array diffraction grating. The scale bar is 20 μm. (b) Zoomed SEM images of the denoted ZrO$_2$ NP patterns with "i" – "vi" in (a). The scale bars are 2 μm.